8-20-2006

Heliospheric Response to Different Possible Interstellar Environments

Hans-Reinhard Muller
Dartmouth College

Priscilla C. Frisch
University of Chicago

Vladimir Florinski
University of California, Riverside

Gary P. Zank
University of California, Riverside

HELIOSPHERIC RESPONSE TO DIFFERENT POSSIBLE INTERSTELLAR ENVIRONMENTS

Hans-Reinhard Müller[1]

Department of Physics and Astronomy, Dartmouth College, 6127 Wilder Laboratory, Hanover, NH 03755; hans.mueller@dartmouth.edu

Priscilla C. Frisch

Department of Astronomy and Astrophysics, University of Chicago, Chicago, IL 60637; frisch@oddjob.uchicago.edu

and

Vladimir Florinski and Gary P. Zank

Institute of Geophysics and Planetary Physics, University of California, Riverside, CA 92521; vladimir.florinski@ucr.edu, gary.zank@ucr.edu

ABSTRACT

At present, the heliosphere is embedded in a warm, low-density interstellar cloud that belongs to a cloud system flowing through the local standard of rest with a velocity near $\sim$18 km s^{-1}. The velocity structure of the nearest interstellar material (ISM), combined with theoretical models of the local interstellar cloud (LIC), suggest that the Sun passes through cloudlets on timescales of $\leq$10^3–10^4 yr, so the heliosphere has been, and will be, exposed to different interstellar environments over time. By means of a multifluid model that treats plasma and neutral hydrogen self-consistently, the interaction of the solar wind with a variety of partially ionized ISM is investigated, with the focus on low-density cloudlets such as are currently near the Sun. Under the assumption that the basic solar wind parameters remain/were as they are today, a range of ISM parameters (from cold neutral to hot ionized, with various densities and velocities) is considered. In response to different interstellar boundary conditions, the heliospheric size and structure change, as does the abundance of interstellar and secondary neutrals in the inner heliosphere, and the cosmic-ray level in the vicinity of Earth. Some empirical relations between interstellar parameters and heliospheric boundary locations, as well as neutral densities, are extracted from the models.

Subject headings: cosmic rays — hydrodynamics — interplanetary medium — ISM: clouds — ISM: structure — stars: winds, outflows

Online material: color figures

1. INTRODUCTION

The heliosphere is a low-density cavity that is carved out from the local interstellar medium (LISM) by the solar wind. The size and particle content of the heliosphere are determined by the solar wind–LISM interaction, and they vary in response to the Galactic environment of the Sun as the Sun and interstellar clouds move through space. The path of the Sun has taken us through the Local Bubble void (Galactic longitudes 180° $\lesssim l \lesssim$ 270°; Frisch & York 1986), and we have recently ($\lesssim$10^3–10^5 yr ago, depending on cloud shapes and densities) entered a clumpy flow of low-density interstellar material (Frisch 1994). This clumpy flow, the cluster of local interstellar cloudlets (CLIC), is flowing away from the Sco-Cen association and extends 10–30 pc into the Galactic center hemisphere and $\lesssim$3 pc for many directions in the anticenter hemisphere. Inhomogeneities in the CLIC create temporal variations in the dynamic interstellar pressure at the solar location, which may produce significant variations in heliosphere properties over geologically short timescales (Frisch 1993, 1997, 2004; Zank & Frisch 1999; Florinski et al. 2003a; Frisch et al. 2005).

The heliosphere itself is a dynamically changing object that is highly sensitive to interstellar pressure (e.g., Holzer 1989; Zank 1999). The interaction of the ISM with the fully ionized solar wind gives rise to the heliospheric morphology, which includes the heliopause (HP), a tangential discontinuity separating solar wind and LISM, and the termination shock (TS), where the solar wind becomes subsonic and is diverted downstream to form a heliotail. Depending on the pressure of the surrounding interstellar material, an interstellar bow shock (BS) may form upwind of the heliopause. These general boundaries are created by the plasma interaction, yet the presence of neutral H and its coupling to the plasma protons via charge exchange greatly influences the details of the heliospheric morphology and the location of its boundaries (see Zank [1999] for a review). The sensitivity of the heliosphere to variations in the physical characteristics of the interstellar cloud surrounding the solar system is poorly understood, and in this paper we focus on heliosphere variations due to encounters with a range of low-density clouds such as those expected in the immediate past and future solar history.

Different interstellar environments may produce noticeable changes in the interplanetary environment of the inner heliosphere, as indicated by the amount of neutral H, anomalous, and Galactic cosmic rays (GCRs) at 1 AU. There is some evidence that lunar soils contain an archive of isotopic abundances that are different from the particle environment of the present era (Wimmer-Schweingruber & Bochsler 2000), and Antarctic ice cores show signatures that may be interpreted as cosmic-ray background variations at Earth (Raisbeck et al. 1987; Sonett et al. 1987; Florinski & Zank 2006). These possibilities have motivated our study of the behavior of the global heliosphere under variable boundary conditions resulting from passage through interstellar clouds.

Given the inhomogeneity of the local solar neighborhood and the Galactic environment in general, we test the heliosphere

---

[1] Also at: Institute of Geophysics and Planetary Physics, University of California, Riverside, CA 92521.

response to a range of local interstellar boundary parameters using about two dozen specific parameter sets. Our choices are justified in § 2. Four highlights of the corresponding heliospheric models are detailed in § 3. The results of all the heliospheric models calculated for this study suggest relationships of the heliospheric boundary locations and the neutral particle densities with the interstellar parameters, discussed in § 4. The synopsis of all the individual model results through these relations is a quantitative expression of the sensitivity of the heliosphere to changing interstellar boundary conditions. Furthermore, the relations allow for a prediction of boundary locations and particle content for heliospheres with arbitrary boundary parameters, without actually engaging in a complex, nonlinear global heliosphere simulation. This predictive power can also be used in the emerging field of astrospheres, which are the analogs of heliospheres around solar-like cool stars.

We discuss the response of the global heliosphere to variable interstellar properties and speculate on aspects of the implications of these variations for the 1 AU location of Earth in § 5.

2. PROPERTIES OF ISM IN THE SOLAR NEIGHBORHOOD

The Sun is embedded in a flow of warm, low-density gas with an upwind direction in the local standard of rest directed toward the Sco-Cen association (Frisch 2004). The CLIC is defined by high-resolution absorption lines toward nearby stars, and lower resolution observations of white dwarf stars in the far ultraviolet (UV) and extreme UV. With the possible exception of α Oph, interstellar column densities toward stars within 35 pc of the Sun do not exceed $\sim 10^{19}$ cm^{-2} (e.g., Frisch 2004; Redfield & Linsky 2004a; Wood et al. 2005b). To date, over 150 absorption components have been identified by velocity in optical and UV observations of at least 90 stars sampling the nearby ISM (see references in Frisch et al. 2002; Redfield & Linsky 2002, 2004a, 2004b). The ISM toward nearby white dwarf stars is partially ionized (Vallerga 1998; Holberg et al. 1999; Frisch 2004), and local variations in $N(\mathrm{Fe}^{+})/N(\mathrm{D}^{0})$ show that the CLIC is inhomogeneous (Frisch 2004). From these data, a general picture has emerged that the ISM within ~ 35 pc of the Sun is dominated by low-density, warm gas. The general properties of this nearby ISM are consistent with partially ionized, low column density gas [$\log N(\mathrm{H}^{0}) < 18$ dex, N in cm^{-2}] described by radiative transfer models (Slavin & Frisch 2002).

2.1. Short-term Variations in the Solar Environment

The properties of the CLIC are diagnosed by Doppler-broadened absorption features representing clouds (or "cloudlets") observed in the optical and UV data toward ~ 100 nearby stars. The best-fitting flow velocity in the local standard of rest (LSR) is -19.4 ± 4.6 km s^{-1}, with an upwind direction $l = 331^\circ.4$, $b = -4^\circ.9$. For comparison, the LSR local interstellar cloud (LIC) velocity is -20.6 km s^{-1}, and the upwind direction is $(l, b) = (317^\circ.8, -0^\circ.5)$. These LSR values assume the standard solar apex motion of 19.7 km s^{-1} toward $l = 57^\circ$, $b = +22^\circ$. The corresponding heliocentric flow vector is -28.1 ± 4.6 km s^{-1} from the upwind direction $(l, b) = (12^\circ.4, 11^\circ.6)$.[2] The flow velocity is somewhat sensitive to the star sample because a velocity gradient between the upwind and downwind directions indicates that the flow is decelerating (Frisch & Slavin 2006).

Data for the nearest cloudlets have been presented in a series of studies by Redfield & Linsky (2002, 2004a, 2004b). Focusing only on UV observations of cloudlets within 15 pc as a predictor of past and future variations in the Galactic environment, we find a range of temperatures T and turbulent velocities ξ: $T = 1700–12,600$ K and $\xi = 0–5.5$ km s^{-1}, with a mean temperature 6780 ± 190 K that compares favorably to the LIC temperature 6300 ± 340 K inferred by spacecraft (Witte 2004). Only $\sim 35\%$ of space within 10 pc of the Sun is filled with neutral gas if this material has the same density as the LIC (~ 0.20 cm^{-3}; Frisch & Slavin 2003) and if $N(\mathrm{D}^{0})/N(\mathrm{H}^{0}) = 1.5 \times 10^{-5}$. The mean cloud lengths are 0.9 ± 0.3 pc. At a relative Sun-cloud velocity of 19 km s^{-1}, such a distance is traversed in $\sim 47,000$ yr. The ISM filling factor $\tilde{f}$ found locally varies from $\tilde{f} \sim 0.60$ toward α Aql (l, b, $d = 47^\circ.7$, $-8^\circ.9$, 5.1 pc), to $\tilde{f} \sim 0.29$ in the opposite direction toward Sirius (l, b, $d = 227^\circ.2$, $-8^\circ.9$, 2.6 pc). Here, $\tilde{f}$ is the fraction of space filled with ISM if all ISM has a density of 0.2 cm^{-3}.

Several sets of data indicate that the ISM within $\sim 3–10$ pc is not uniform. The ratio $N(\mathrm{Fe}^{+})/N(\mathrm{D}^{0})$ varies between the downwind and upwind LSR directions by up to a factor of ~ 8, apparently from ionization or abundance variations (Frisch 2004). The ISM temperature within 5 pc varies by over a factor of 4 (Redfield & Linsky 2004b). If the cloud in front of the nearest star α Cen also extends in front of α Oph, as indicated by their common velocity, and is uniform, then Ca^{+} and H^{0} data suggest a density $n > 5$ cm^{-3} (Frisch 2003), in contrast to the LIC density ~ 0.3 cm^{-3}. Velocity variations of 10 km s^{-1} or more are also found along several individual sight lines (Frisch et al. 2002; Redfield & Linsky 2004b).

A series of radiative transfer models appropriate for the radiation field and physical properties of the low column density material close to the Sun show that equilibrium occurs for a range of ionization levels in low-density ISM (Slavin & Frisch 2002; Frisch & Slavin 2006). Furthermore, the boundary conditions of the heliosphere will vary as it traverses low-density ISM strictly because of ionization variations within the cloud. These models generally consider clouds with $n_{\mathrm{tot}} \lesssim 0.3$ cm^{-3}, $N(\mathrm{H}^{0}) < 10^{18}$ cm^{-2}, a local radiation field consistent with observations of the diffuse radiation field between 3000 Å and 0.5 keV at the solar location, and allow for additional radiation emitted by a possibly magnetized conductive interface between the local warm gas and adjacent very hot Local Bubble plasma. These models predict ISM equilibrium conditions for $n(\mathrm{H}^{0}) = 0.16–0.26$ cm^{-3}, hydrogen ionization levels $\chi(\mathrm{H}) = \mathrm{H}^{+}/(\mathrm{H}^{0} + \mathrm{H}^{+}) = 0.19–0.34$, and cloud temperatures of 4900–8300 K.

The time of the Sun's entry into, and exit from, the LIC can be estimated using observations of H^{0} and D^{0} toward nearby stars combined with $n(\mathrm{H}^{0})$ derived from the Slavin & Frisch radiative transfer models. These models of the LIC indicate that $n(\mathrm{H}^{0}) = 0.19–0.21$ cm^{-3} and $n(\mathrm{H}^{+}) \sim 0.1$ cm^{-3} at the solar location, and that $n(\mathrm{H}^{0})$ decreases by $<20\%$ between the Sun and surface of the LIC. Assuming a constant LIC density of $n(\mathrm{H}^{0}) = 0.2$ cm^{-3} and using the limits on the LIC component toward 36 Oph [$N(\mathrm{H}^{0}) < 6 \times 10^{16}$ cm^{-2}; Wood et al. 2000a], we infer that the distance to the LIC surface in this direction, as defined by a velocity discontinuity in the gas, is <0.1 pc, suggesting that the Sun will exit the LIC in less than 3700 yr.

The entry of the Sun into the LIC can be calculated after transforming into the LSR frame and assuming a LIC morphology (e.g., Frisch 1994). If the LIC velocity vector is perpendicular to the surface, and assuming $N(\mathrm{H}^{0}) = 4.0 \times 10^{17}$ cm^{-2} toward α CMa (Hebrard et al. 1999), the Sun would have entered the LIC ~ 6700 (11,500) yr ago for the *Hipparcos* (standard) solar apex

---

[2] An alternate solar apex motion, based on *Hipparcos* data (13.4 km s^{-1} toward $l = 27^\circ.7$, $b = 32^\circ.4$; Dehnen & Binney 1998) yields an LSR bulk flow velocity -17.0 ± 4.6 km s^{-1} with upwind direction $(l, b) = (2^\circ.3, -5^\circ.2)$, and an LSR LIC vector of -15.7 km s^{-1}, upwind $(l, b) = (346^\circ.0, 0^\circ.1)$.

motion. The assumed column density requires additional ISM near the LIC velocity toward the downwind stars α Aur and χ^1 Ori. Alternatively, the LIC column densities toward downwind stars can be used to define a plane that advances through space with the LIC velocity vector. The useful downwind stars for this estimate are α CMa, α CMi, χ^1 Ori, and α Aur, for which column densities for the LIC are, respectively, $\log N(H^0) = 17.60$, 17.90, 17.80, and 18.26 cm^{-2} based on D/H $= 1.5 \times 10^{-5}$ and data by Hebrard et al. (1999) and Redfield & Linsky (2004a); the selection of any three of these four stars, and assuming $n(H^0) = 0.2$ cm^{-3}, suggests that the Sun entered the LIC about 28,000–30,250 yr ago. When uncertainties of $\sim$30% are incorporated to reflect the various assumptions, these estimates suggest that the Sun has entered the interstellar cloud component at the LIC velocity sometime within the past 40,000 yr and will exit it sometime within the next 4000 yr.

The star χ^1 Ori is within 15° of the downwind direction and shows a cloud with a relative Sun-cloud velocity of 21.6 km s^{-1}. The Sun and this cloud would have first crossed paths $\sim$47,000 yr ago for $n(H^0) = 0.2$ cm^{-3}. Beyond χ^1 Ori, the next neutral gas in the downwind direction is over 50 pc away. Allowing for $\sim$30% uncertainties and possible gaps between clouds, the Sun would have entered the CLIC within the past $\sim$60,000/$\tilde{f}$ yr.

2.2. *Variations in the Global ISM*

An ISM with a wide range of properties is found within $\sim$350 pc of the Sun, including low-density, hot gas in the Local Bubble that emits soft X-rays. UV and radio observations of low column density ISM show that a range of ISM types are possible at low column densities. The ISM within that distance provides a model for the types of ISM the Sun may encounter over timescales of several million years. The Sun will move $\gtrsim$16–20 pc through the LSR per million years, and interstellar clouds (with velocities of up to $\gtrsim$100 km s^{-1}) may move hundreds of parsecs.[3]

One example for ISM structure in this range is provided by Welty et al. (1999), who compared optical and UV ISM data for the star 23 Ori (300 pc), which is in the direction of the Ori-Eri soft X-ray superbubble, and found a complex system of cloudlets showing a wide range of properties representing typical diffuse ISM. Twenty-one cloudlets with LSR velocities that range from -120 to $+8$ km s^{-1} are found. Four low-velocity clouds (positive V_{LSR}) at $\sim$100 K are present. They are massive [$\log N(H) = 20.7$ cm^{-2}] and moderately dense (10–15 cm^{-3}), suggesting a cloud thickness of $\lesssim$15 pc, and primarily neutral. Crossing such a cloud might take the Sun $\sim$1 Myr. Warmer dense clouds ($\sim$15–20 cm^{-3}, primarily neutral, $\sim$3000 K) with thicknesses $\lesssim$1 pc are found at moderately low velocities ($V_{LSR} \sim -17 \rightarrow 0$ km s^{-1}). At higher velocities ($V_{LSR} \sim -60 \rightarrow -17$ km s^{-1}) low-density gas [$n(H^0) = 1$–6 cm^{-3}] is found. This material appears to be in thin sheets with thicknesses of 0.001–0.04 pc. Warm ($\sim$8000 $\pm$ 2000 K), rapidly moving ($V_{LSR} = -130 \rightarrow -100$ km s^{-1}) shocked low column density clouds are also seen. This gas is partially ionized [$n(e^-) = n(H^0) = 0.4$–0.5 cm^{-3}] and arises in clouds with thicknesses of about 0.005–0.12 pc. The ionization of this high-velocity gas suggests an interstellar radiative shock where the gas is not in ionization equilibrium (since the collisionally ionized species show $T \sim 25,000$ K, but Doppler b-values indicate 6000–12,000 K).

The Millennium Arecibo H^0 21 cm radio survey of warm neutral material (WNM) and cold neutral material (CNM) also provides a comparison sample for the CLIC (Heiles & Troland

---

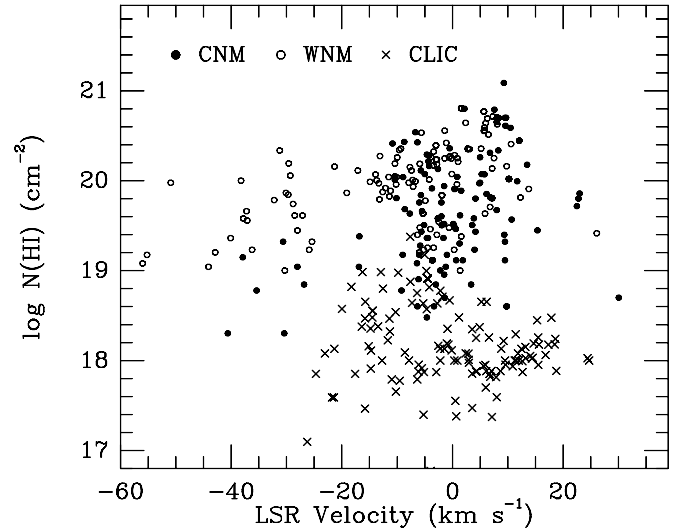[3] A velocity of 1 km s^{-1} corresponds to $\sim$1 pc Myr^{-1}.

Fig. 1.—Velocity distribution of the CLIC vs. CNM and WNM: the CLIC components are plotted with crosses. The CLIC components shown here are toward stars within 50 pc. The LSR velocities are derived from H^0, D^0, and optical Ca$^+$ data in Frisch et al. (2002), Redfield & Linsky (2002, 2004a), and Wood et al. (2005b) (standard solar apex motion used). Points based on $N(D^0)$ [or $N(Ca^+)$] data assume $N(D^0)/N(H^0) = 1.5 \times 10^{-5}$ [or $N(Ca^+)/N(H^0) = 1.0 \times 10^{-8}$]. Filled and open circles show the CNM and WNM H^0 components, respectively (from Heiles & Troland 2003a). Only high-latitude H I sight lines are included ($|b| > 25°$). Note that the CNM and WNM data sample may contain non-local components with velocities affected by differential Galactic rotation. By selecting the high-latitude H I sight lines, the sample is more likely restricted to nearby regions, where Galactic rotation effects make minimal contributions to the CNM and WNM component velocities.

2003a, 2003b). Figure 1 shows the LSR velocities of CLIC components observed in the optical and UV (data from Frisch et al. 2002; Redfield & Linsky 2004a, 2004b; Wood et al. 2005b) compared to CNM and WNM velocities. Except for extra-high-latitude infalling ISM flows at $v < -25$ km s^{-1} (Lockman & Gehman 1991), the kinematics of the CLIC is similar to WNM and CNM. If viewed from the outside, the CLIC would appear as a medium-velocity flow (17–20 km s^{-1}) with low column densities [$N(H^0) < 10^{19}$ cm^{-2}]. The WNM has upper-limit kinetic temperatures of 500 K to over 10,000 K, and median column densities of 1.3×10^{20} cm^{-2}. The dominance of low-mass warm clouds at intermediate velocities (< -17 km s^{-1}) seen in Figure 1, combined with the fact that $\sim$60% of the H^0 is WNM, suggest that warm, low density clouds are the most likely to be encountered by the Sun over the next million years.

The recent discovery of cold ($<$100 K) tiny neutral cloudlets in the ISM, $N(H^0) \sim 10^{18}$ cm^{-2}, including one toward 3C 286 at a velocity within 1.5 km s^{-1} of the G-cloud velocity (Stanimirović & Heiles 2005), shows that tiny cold neutral clouds are widespread but infrequent. CNM components with $N(H^0) \lesssim 10^{18}$ cm^{-2} and densities $\sim$20 cm^{-3}, similar to values found by Welty et al. (1999) toward 23 Ori, would have thicknesses of $<$0.02 pc and if at rest in the LSR would perturb the heliosphere boundary conditions on timescales of $\sim$100 yr.

2.3. *Modeled Clouds*

The above discussion of the ISM in the solar neighborhood, and close to the Sun, provides the basis for selecting a representative set of boundary conditions for modeling. The heliosphere configuration has been modeled for 27 cloud types with densities varying from 0.005 to 15 cm^{-3}, ionizations ranging up to 100%, and relative Sun-cloud velocities of up to 100 km s^{-1}. The boundary parameters are listed in Table 1. Most of the assumed cloud

TABLE 1
MODEL BOUNDARY PARAMETERS

No.	n_{H^0} (cm^{-3})	n_{H^+} (cm^{-3})	n_{tot} (cm^{-3})	$\chi(H)$	v_{LISM} (km s^{-1})	T_{LISM} (K)
1	0.00	0.005	0.005	1.00	13.4	1260000
2	0.14	0.10	0.24	0.42	8.3	7000
3	0.24	0.04	0.28	0.14	15	3000
4	0.24	0.04	0.28	0.14	26	7000
5	0.216	0.047	0.26	0.18	26	7000
6	0.242	0.074	0.32	0.23	26	7000
7	0.24	0.10	0.34	0.29	26	7000
8	0.235	0.106	0.34	0.31	26	7000
9	0.14	0.10	0.24	0.42	25	5650
10	0.14	0.10	0.24	0.42	26	8000
11	0.04	0.04	0.08	0.50	15	3000
12	0.04	0.04	0.08	0.50	26	7000
13	0.10	0.10	0.20	0.50	26	8000
14	0.40	0.40	0.80	0.50	100	8000
15	11.00	0.15	11.15	0.01	26	100
16	15.00	0.20	15.20	0.01	26	10
17	15.00	0.20	15.20	0.01	26	3000
18	0.14	0.10	0.24	0.42	31.5	5650
19	0.14	0.10	0.24	0.42	37.7	5650
20	0.14	0.10	0.24	0.42	45.2	7000
21	0.14	0.10	0.24	0.42	50.8	7000
22[a]	0.14	0.10	0.24	0.42	68	8000
25	0.14	0.10	0.24	0.42	86	8000
26	0.24	0.04	0.28	0.14	50.8	10
27	0.96	0.04	1.00	0.04	50.8	10

[a] Model 23: $T_{SW} = 2 \times 10^5$ K. Model 24: $v_{SW} = 500$ km s^{-1}.

types are warm and low-density clouds, but the possible velocities vary by an order of magnitude. The Sun moves through the LSR at $\sim$14–19.5 km s^{-1}, while warm diffuse clouds have LSR velocities 20–60 km s^{-1} and higher. In particular, the cloud cluster near the Sun shows depletions characteristic of shocked interstellar gas (Frisch 1981, 2004), for which large peculiar motions might be expected. Hence, relative Sun-cloud velocities may range over an order of magnitude, leading to appreciable variations in the heliosphere morphology.

Table 1 gives the LISM boundary conditions as neutral hydrogen number density $n(H^0)$, proton number density $n(H^+)$, and heliocentric velocity v_{LISM} and temperature T_{LISM} of the interstellar wind; n_{tot} is the total hydrogen density, and $\chi(H) = n(H^+)/n_{tot}$ is the interstellar hydrogen ionization fraction. Model 1 [$n_{tot} = 0.005$ cm^{-3}, $\chi(H) = 1$, $v = 13.4$ km s^{-1}, log $T = 6.1$ K] represents the hot plasma interior of the Local Bubble (Snowden et al. 1997). Model 2 also tests subsonic interstellar conditions, but with a 42% partially ionized dense, warm ISM ($n_{tot} = 0.24$ cm^{-3}, $T = 7000$ K). The velocity in model 2 (8.3 km s^{-1}) is comparable to the heliocentric velocity of the blueshifted cloud found toward ϵ CMa and α CMa (Gry & Jenkins 2001), which may have been the first warm cloud encountered by the Sun as it exited the plasma interior of the Local Bubble.

Models 3–10 test the effect of small density ($n_{tot} = 0.24$– 0.34 cm^{-3}), warm-temperature (3000–8000 K), and velocity (15–26 km s^{-1}) variations on the heliosphere morphology, with varying ionizations [$\chi(H) = 0.14$–0.42], representing the warm, low-density ISM described earlier. Neutral clouds with $T \sim$ 3000 K are widespread and evidently thermally unstable in the absence of magnetic pressure (Heiles 2001). Models 4–10, with $v \sim 26$ km s^{-1}, represent variants of the contemporary heliosphere whose interstellar boundary densities fall within the constraints of the observations. Model 9 corresponds to the α Cen

environment (Linsky & Wood 1996; Wood et al. 2001), provided the ISM spreads uniformly throughout the sight line toward this nearest star. Model 10 is based on the local cloud toward the white dwarf star RE J1032+532 (Holberg et al. 1999).

Models 11–14 represent the effect on the heliosphere of density ($n_{tot} = 0.08$–0.8 cm^{-3}) and velocity (15–100 km s^{-1}) variations in 50% ionized interstellar hydrogen at warm temperatures (3000–8000 K), such as might be expected for kinematically perturbed low-density gas. Models 15–17 test the expected dramatic differences in heliosphere configuration anticipated from the encounter with a denser ($n_{tot} = 11$–15 cm^{-3}), neutral [$\chi(H) = 0.01$], cold, or tepid ($T = 10$–3000 K) interstellar cloud at the LIC velocity. Model 15 is based on the strong-line, low-velocity gas toward 23 Ori (Welty et al. 1999), while model 17 is based on both the warm, low-velocity gas toward 23 Ori and the thermally unstable warm H^0 gas observed at 21 cm (Heiles 2001). Model 16 was calculated solely for comparison with model 17, representing a temperature reduction by a factor of 300 without a corresponding density increase that typical Galactic values of the roughly constant product $n_{tot}T_{LISM}$ would suggest.

Models 18–25, together with 2, test the parameter space around a partially ionized, diffuse interstellar cloud [$\chi(H) = 0.42$; $n_{tot} = 0.24$ cm^{-3}], sampling velocity variations from 8 to 100 km s^{-1}. Changes that arise from small variations in the solar wind are also considered (models 23 and 24). Model 14 is an example of cooled high-velocity shocked gas, such as a superbubble shell formed from a supernova shock sweeping up the ISM in a star-forming region. Its parameters are based on high-velocity gas observed toward 23 Ori and ζ Ori (Welty et al. 1999, 2002). Finally, models 26–27 test a cold (10 K), high-velocity (51 km s^{-1}) regime, again at lower values of $n_{tot}T_{LISM}$ than typically encountered, in order to discuss low-temperature regimes without getting into the complications of very high density heliospheres.

3. INDIVIDUAL MODEL RESULTS

To characterize the large-scale heliospheres that result when the Sun is embedded in the different parts of the ISM as described above, we make use of the multifluid model developed by Zank et al. (1996b). The multifluid code simultaneously solves the time evolution of four interpenetrating fluids. One fluid represents the protons of the interstellar plasma component, as well as the solar wind plasma. The remaining fluids model three thermodynamically distinct populations of neutral H. Each of the neutral fluids interacts with the plasma through resonant charge exchange, using the Fite et al. (1962) cross section, and all neutrals are subjected to photoionization, which depends on the squared distance to the Sun. Radiation pressure is assumed to balance gravity. For a detailed description of the numerical model and the underlying physics, see Zank et al. (1996b) and Zank (1999).

Modeling of heliospheric neutrals in the multifluid code as a superposition of three independent neutral fluids is an approximation to the general, non-Maxwellian neutral distribution function. Neutrals can also be calculated on a kinetic level without such an approximation (e.g., Baranov & Malama 1993; Müller et al. 2000). Recent comparison studies (Alexashov & Izmodenov 2005; Heerikhuisen et al. 2006) have shown that the multifluid and kinetic methods are in essential agreement in most of the fine details concerning heliospheric geometry and shock locations, and even the distributions look similar. For this reason, we adhere to the computationally less costly multifluid method for this study.

For the numerical models, the solar wind at 1 AU is assumed to be independent of longitude, latitude, and time, with values of 5.0 cm^{-3} for the plasma density, a temperature of 10^5 K, and a

radial velocity of 400 km s^{-1}. There are two models (23 and 24) with slight variations on these solar wind conditions (2×10^5 K and 500 km s^{-1}, respectively). The models of the interaction of the solar wind with the ISM are carried out in a heliocentric frame of reference and are effectively two-dimensional, as we assume azimuthal symmetry about the stagnation axis (the axis parallel to the LISM flow that contains the Sun). To satisfy this assumption, we also neglect heliospheric and interstellar magnetic fields. The interstellar medium is prescribed as four boundary conditions at a suitably large distance from the Sun (a typical value is 1000 AU for heliospheres for which the interstellar bow shock is less than 500 AU from the Sun). The boundary parameters are the LISM H^0 and H$^+$ number densities, and the (common) hydrogen velocity and temperature.

3.1. *Contemporary LISM*

Inferred values of the contemporary interstellar boundary parameters are $v = 26.3$ km s^{-1} and $T \sim 6300 \pm 340$ K (Witte et al. 1996; Witte 2004). The contemporary interstellar proton and neutral H densities are not well constrained but should lie in the ranges 0.04–0.14 cm^{-3} and 0.14–0.24 cm^{-3}, respectively (e.g., Zank 1999; Slavin & Frisch 2002), and models 4–10 (Table 1) fit within these contemporary constraints. We choose model 5 [$n(\mathrm{H}^+) = 0.047$ cm^{-3}, $n(\mathrm{H}^0) = 0.216$ cm^{-3}, $v = 26$ km s^{-1}, and $T = 7000$ K] as the highlighted example representing the contemporary heliosphere. This model has been described in some detail previously by Müller & Zank (2004), whose Figure 1 displays two-dimensional maps of plasma temperature and neutral density, featuring this model's heliospheric boundaries together with the neutral hydrogen wall. Here, we do not repeat this figure, but rather display the plasma temperature (*top panel*) and density (*bottom panel*) along the stagnation axis as solid lines in Figure 2, together with the neutral H density (*double-dot-dashed line*).

The heliospheric boundaries are clearly visible as discontinuities in Figure 2, and labels are provided next to the temperature profile. The solar wind is supersonic at 1 AU and expands radially before undergoing a transition (temperature and density increase) at the TS. The TS is asymmetric, with a nose distance of 99 AU and a tail distance of 216 AU. In the heliosheath, the region of the shocked and heated solar wind, the solar wind plasma gets directed tailward and is separated from the interstellar plasma by the HP, with discontinuous density and temperature. The stagnation point (the nose of the HP) is at 148 AU. The LISM is supersonic and consequently there is an interstellar BS at 285 AU upwind.

The thermodynamically distinct plasma regions define the characteristics of the three neutral fluids used in the four-fluid model. The component 1 neutral population consists of neutrals from the ISM. They typically are warm and of moderate bulk speed. Neutrals born through charge exchange in the hot heliosheath between the TS and the HP form a different neutral population (component 2), which is hot, with correspondingly high thermal speeds. The third component consists of neutrals born inside the TS in the supersonic solar wind; correspondingly, component 3 neutrals are fast and warm. While the approximation of the real neutral distribution function throughout the heliosphere by a superposition of three Maxwellians (the three neutral fluids) introduces inaccuracies into the models, such a hydrodynamic treatment represents the overall neutral H distribution well, as evidenced, for example, by the successful matching of modeled and observed Lyα absorption by heliospheric H^0 (Wood et al. 2000b).

Figure 2 also shows the temperature and density profile of a plasma-only model (model 1, *dashed lines*, TS at 90 AU, HP at
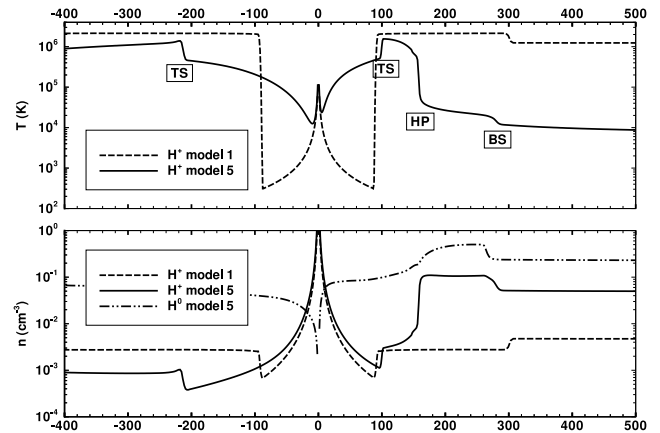
Fig. 2.—One-dimensional profiles along the stagnation axis, with the Sun at center and the LISM coming from the right. *Top*: Plasma temperature of model 1 (the Local Bubble case; *dashed line*) and model 5 (representing contemporary conditions; *solid line*). The heliospheric boundaries of model 5 are marked in the plot. *Bottom*: The corresponding densities (plasma model 1, *dashed line*; plasma model 5, *solid line*; model 5, neutral H, *double-dot-dashed line*). [*See the electronic edition of the Journal for a color version of this figure.*]

300 AU), which is described in detail in § 3.2. The contrast between the two plasma temperature profiles is due to the effect of charge exchange: the pickup process (here, the charge exchange of a solar wind proton with an interstellar neutral H atom in the supersonic solar wind region) deposits energy into the supersonic solar wind and reverses the effect of adiabatic cooling (and also slows the solar wind), such that the effective solar wind temperature of model 5 turns upward, whereas model 1 follows an adiabatic cooling law. In both inner and outer heliosheath, heat transport by neutral hydrogen with subsequent secondary charge exchange introduces gradual temperature gradients between the discontinuities that are absent in model 1, which has no neutrals, no charge exchange, and no anomalous heat transport across the HP.

In the contemporary heliosphere (model 5), there is a hydrogen wall between the BS and the HP, with a peak density of 0.502 cm$^{-3} = 2.3 n(\mathrm{H}^0)$ (Fig. 2, *bottom panel, double-dot-dashed line*). The extra wall material consists of slower neutral hydrogen born from charge exchange with the subsonic interstellar plasma downstream of the BS (the outer heliosheath). The outer heliosheath plasma is interstellar plasma that is slowed and heated at the BS and further affected by additional momentum loss and energy gain through charge exchange of component 2 neutrals that cross from the inner into the outer heliosheath. The hydrogen wall is accompanied by an elevated plasma density (Fig. 2, *bottom panel, solid line*) because of the plasma slowdown.

The neutral atom density at the upwind TS is 0.098 cm$^{-3} = 0.46 n(\mathrm{H}^0)$, the latter ratio being called the filtration factor because it links the interstellar density to the neutral density in the inner heliosphere, accounting for the loss processes along its path. The neutral density at 5 AU on the upwind stagnation axis is 0.036 cm$^{-3} = 0.17 n(\mathrm{H}^0)$. Closer to the Sun, photoionization and solar wind charge exchange deplete neutral H exponentially. In the tail direction, the stagnation axis repopulates slowly with off-axis neutral H.

Models 4–10 of Table 1 loosely fit within the constraints of contemporary observations and generally represent ionization and density levels appropriate for low column density ISM where both radiation field and abundances of cooling trace elements might vary. Table 2 gives the corresponding results for all models, and it can be seen that the results from models 4–10 only vary modestly.

TABLE 2
Model Results

No.	TS (AU)	HP (AU)	BS (AU)	TS_d (AU)	f_{peak}	f_{TS}	$f_{5\,AU}$
1........	90	300	...	90	...	...	...
2........	259	402	...	371	1.1	0.12	0.04
3........	149	233	535	286	2.1	0.29	0.10
4........	85	132	225	191	2.3	0.54	0.23
5........	99	148	285	216	2.3	0.46	0.17
6........	74	115	198	164	2.3	0.40	0.20
7........	83	110	250	178	2.4	0.38	0.13
8........	69	100	186	152	2.4	0.37	0.16
9........	99	137	280	207	2.5	0.29	0.10
10........	79	104	230	166	2.3	0.40	0.17
11........	253	358	812	463	2.1	0.28	0.08
12........	144	197	365	331	2.4	0.50	0.18
13........	86	119	242	180	2.3	0.39	0.17
14........	11	14	21	52	3.3	0.82	0.60
15........	14	26	100	37	3.0	0.12	0.08
16........	8.2	12	23	28	7.0	0.14	0.10
17........	9.8	16	34	23	3.1	0.12	0.09
18........	91	126	227	227	2.9	0.35	0.12
19........	62	85	136	173	3.2	0.50	0.21
20........	52	69	108	159	3.3	0.59	0.26
21........	45	62	92	152	3.5	0.68	0.31
22........	32	44	63	122	2.8	0.97	0.51
23........	32	44	63	121	2.9	0.96	0.52
24........	39	54	79	139	3.0	0.82	0.42
25........	26	34	50	112	2.7	1.00	0.64
26........	38	44	77	141	5.3	0.87	0.25
27........	21	31	46	72	3.4	0.88	0.54

The size of the heliosphere changes, with HP locations ranging from 100 to 150 AU, and neutral hydrogen filtration varies from 0.3 to 0.5, while the relative peak wall density remains essentially unchanged.

3.2. Hot Local Bubble

The interior of the Local Bubble void is hot and nearly completely ionized. The absence of interstellar neutral hydrogen in model 1 simplifies the heliospheric physics considerably, because in all other models the atom-ion process of charge exchange generates distinct features in the atom distribution function and also alters the plasma by coupling ions and atoms.

We adopt the ISM parameters of $n(H^+) = 0.005$ cm^{-3}, $n(H^0) = 0$, $v = 13.4$ km s^{-1}, and $\log T(K) = 6.1$ (model 1 in Table 1), with the velocity based on the Dehnen & Binney (1998) solar apex motion, since the plasma is assumed at rest in the LSR. The speed of sound in such a plasma is 190 km s^{-1}, and the Sun therefore moves subsonically through this medium (Mach 0.07). In this case, the isotropic thermal interstellar pressure dominates the ram pressure, and the termination shock is spherical at a distance of 90 AU from the Sun. This distance is comparable to that of the contemporary heliosphere. The distance to the nose of the heliopause is 300 AU, which makes this sheath very large in comparison to the contemporary heliosphere above. The temperature in the sheath reaches values as high as 2.2×10^6 K. Figure 2 contains the plasma temperature profile (top panel) along the stagnation axis, and the plasma density (bottom panel), as dashed lines. In the termination shock transition, the density jumps by a factor of 3.8, and the wind speed decreases to 100 km s^{-1}.

In this model there are no neutral atoms in the entire system of solar wind and interstellar medium, and hence the particle content is different from that observed today. There are no pickup ions

(PUI) produced by charge exchange, and therefore there are no anomalous cosmic rays, and no slowdown or heating in the supersonic solar wind beyond the inner solar system. However, thanks to its large ram pressure the solar wind plasma still provides an effective shield of the solar system against the million-degree plasma of the Local Bubble.

As a plasma-only model with subsonic interstellar boundary conditions, model 1 is ideally suited for comparison to previous, analytical studies of the heliosphere under the assumption of incompressibility of the flow outside of the TS. For the simple case of a flow around a rigid sphere (as a stand-in for the heliopause), the interstellar velocity on the stagnation axis behaves as $v_\infty(1 - r_{HP}^3/r^3)$, where r_{HP} is the distance to the HP nose, and v_∞ is the uncontaminated interstellar flow velocity. This analytical behavior matches the one of model 1 very well (figure not shown here). In a detailed treatment, Suess & Nerney (1990) calculated the flow streamlines from a realistic, pressure-balanced TS outward. Their TS distance formula (eq. [7]) predicts it to be at 81.8 AU, which compares well with the 90 AU found in model 1, given that the latter (numerical) model does not presuppose incompressibility.

It has to be noted that the models do not account for the interplanetary magnetic field, as doing so requires a three-dimensional treatment of the problem that is outside the scope of this paper. In particular for model 1 in which the mitigating aspects of the neutral-plasma interaction are absent, the pile-up of magnetic field at the nose of the HP (Axford-Cranfill effect; e.g., Nerney et al. 1993) may be a contributor to the overall pressure balance in the upwind directions of the inner heliosheath. The plasma would not decelerate as quickly as $1/r^2$ downstream of the TS, as is approximately the case in model 1. Consequently, the heliopause would be expected to shift farther away than the location identified in this paper. The unknown interstellar magnetic field strength in the Local Bubble has the potential to shift the pressure balance of the heliosphere as well.

3.3. Dense ISM

Three models in Table 1 represent the effect of an ISM that is denser than that of the contemporary heliosphere by a factor of ~50 (models 15–17), but not as dense as models investigated by Yeghikyan & Fahr (2003) with $n_{tot} = 100$ cm^{-3}. In addition, models 14 and 27 are denser by a factor of 3–4 above the contemporary value. The high density leads to a high interstellar ram pressure, and therefore the resulting heliosphere tends to be smaller.

As an example, Figure 3 displays two-dimensional maps of the hydrogen density and plasma temperature of model 17 [$n(H^0) = 15$ cm^{-3}], and Figure 4 shows stagnation axis temperature, density, and velocity profiles (dashed lines). The TS is asymmetric with a nose distance of 9.8 AU and a tail distance of 23 AU (Table 2). The HP is located at 16 AU, and the BS is at 34 AU upwind. The TS is weak, with an upwind compression ratio of 1.8. Atypically, the HP is not a sharp temperature gradient as in most other models, but the temperature profile is more washed out by frequent charge exchange. The bow shock has a moderate compression ratio of 3.

In spite of the small heliosphere, neutrals and protons are coupled tightly because of the high neutral density so that the hydrogen wall starts immediately downstream of the BS. It has a peak density of $3.1 n(H^0)$, but charge exchange is frequent enough that the neutral density at the TS (the filtration factor) is $0.12 n(H^0)$, which is among the lowest of the 27 models considered here. Even so, the absolute neutral density is quite high, leading to a pronounced solar wind slowdown. On the upwind stagnation axis,
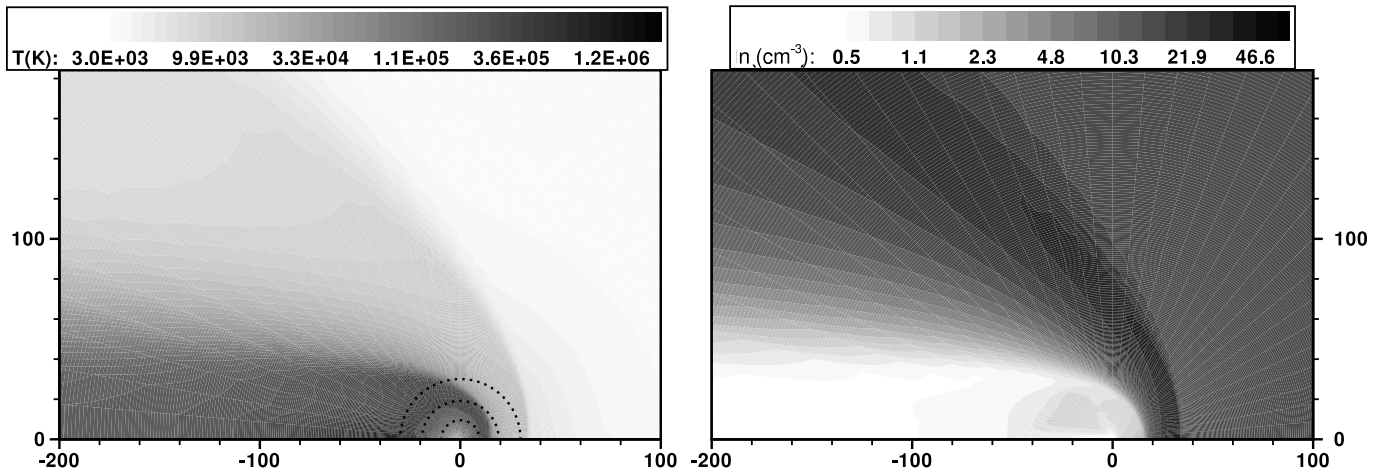
FIG. 3.—Two-dimensional maps of plasma temperature (*left*) and neutral H density (*right*) for the high-density case 17, with the Sun at center and the LISM coming from the right. The transition from white to medium gray in the plasma temperature is the interstellar bow shock; the dark shades are the hot heliosheath and heliotail. The orbits of Saturn, Uranus, and Neptune are sketched as dotted lines. [*See the electronic edition of the Journal for a color version of this figure.*]

the solar wind speed decreases to 260 km s^{-1} upstream of the TS. In the tail region, the solar wind plasma slows to 160 km s^{-1}, but frequent charge exchange decreases that value in the heliotail to a common plasma/neutral speed of $\sim$60 km s^{-1} by $\sim$100 AU downwind of the Sun.

3.4. High-velocity ISM

Several models in Table 1 test the response of the heliosphere on which a high-velocity ISM impinges (models 14 and 18–27). The high velocity generates a large ram pressure, making the resulting heliosphere smaller, similar to, but more elongated than, the high-density cases. We present model 25 with $v = 86$ km s^{-1} in more detail here. If the corresponding cloud had a thickness
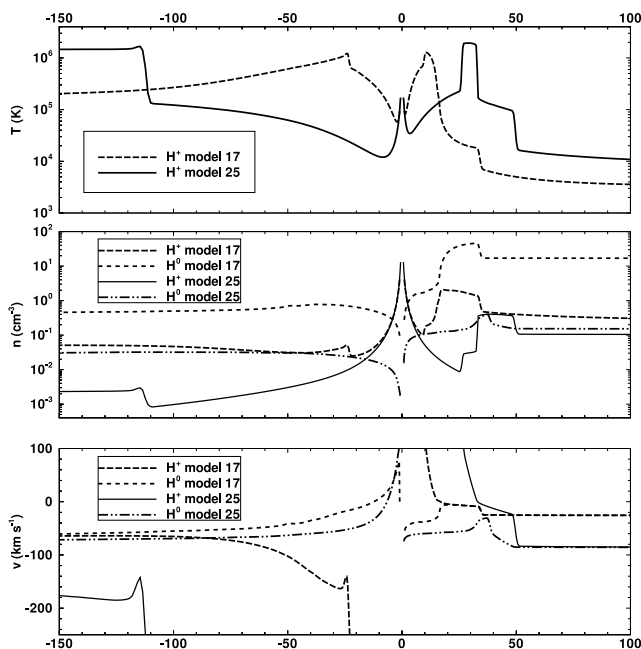

FIG. 4.—Similar to Fig. 2; one-dimensional profiles of plasma temperatures (*top*), number densities (*middle*), and parallel velocities (*bottom*) for model 17 (high-density case; *long- and short-dashed lines*) and model 25 (high-velocity case; *solid and double-dot-dashed lines*). [*See the electronic edition of the Journal for a color version of this figure.*]

comparable to the high-velocity ISM toward 23 Ori ($<$0.12 pc, § 2.2), it would pass over the Sun in less than $\sim$1400 yr. Figure 5 displays two-dimensional maps of hydrogen density and plasma temperature of model 25, showing the heliospheric boundaries and features clearly. The one-dimensional stagnation axis profiles in temperature, density, and velocity are displayed in Figure 4.

In most models, the TS, taken as a three-dimensional surface, is spherical (model 1) or nearly spherical with an upwind/downwind asymmetry. These cases are characterized by a heliosheath and heliotail plasma that are subsonic throughout. In contrast to this, the shape of the TS of a high-velocity ISM heliosphere, such as model 25, is qualitatively different, now resembling a rocket shape. The initially subsonic plasma at the nose of the heliosheath accelerates to supersonic speeds in the nozzle-shaped region between the TS and the HP. However, to match the subsonic heliotail plasma and the supersonic heliosheath plasma requires both a shock to decelerate the flow and a tangential discontinuity to adjust the density. A characteristic triple point occurs where heliosheath shock, termination shock, and the tangential discontinuity meet. Figure 5 shows this morphology in the example of model 25.

The TS is highly asymmetric, with a nose distance of 26 AU and a tail distance of 112 AU (Table 2). The upwind TS compression ratio s is $s = 2.9$. The HP is at 34 AU, and the BS is at 50 AU upwind. The bow shock is quite strong, with a post-shock plasma speed of 24 km s^{-1} (Fig. 4, *bottom panel*), temperature of 10^5 K (*top panel*), and a compression ratio of 3.4 (*middle panel*). Because of the large neutral velocity in the post-bow-shock region, the neutral mean free path (MFP) for charge exchange is initially $\sim$30 AU, larger than the outer heliosheath, and shortens only gradually as the effective neutral velocity decreases to 31 km s^{-1}. Consequently, the model 25 hydrogen wall between the BS and the HP is not very thick, but reaches a peak density of $2.7n(H^0)$ about $\sim$11 AU downstream of the BS. This distance from the BS is of the same magnitude as in the more moderate cases; however, in the high-speed case, it brings the peak close to the HP already. As the TS is so close to the hydrogen wall, the filtration factor is 1.0; i.e., the neutral density at the TS equals that of the LISM [and is still $0.6n(H^0)$ at 5 AU; Fig. 4, *middle panel*]. These filtration factors close to unity (models 14 and 22–27 in Table 2) seem only possible when a high interstellar velocity combines with a modest or low density so that the peak hydrogen wall
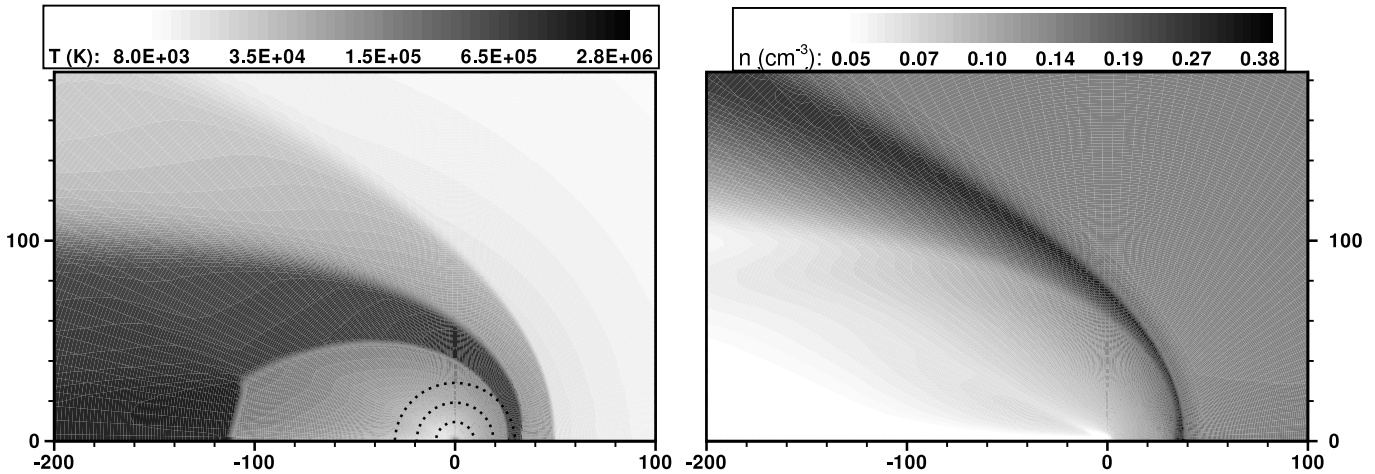
Fig. 5.—Two-dimensional maps of plasma temperature (*left*) and neutral H density (*right*) for the high-speed case 25. Note the triple point at about $(-105, 30)$. The orbits of Saturn, Uranus, and Neptune are sketched as dotted lines. In the neutral density (*right*), the hydrogen wall is clearly visible. [*See the electronic edition of the Journal for a color version of this figure.*]

occurs close to the HP without room for depletion of neutral H between peak and HP. In the similar-sized dense heliosphere (§ 3.3), the charge-exchange MFPs are shorter, the peak hydrogen wall is attained farther away from the HP, and charge exchange upwind close to the HP spreads the H flow and leads to a density decrease already before the H^0 flow crosses the HP (Fig. 4).

Finally, we note that for the high-speed models 14 and 22–27, the original numerical grid with a $5°$ angular resolution is too coarse, leading to errors during the transport along directions with high-velocity components. In these cases, we choose a grid with a $2°$ angular resolution, which cures the problem so that pre-BS density values on the stagnation axis are within 10% or better of the LISM values. They are always more accurate in off-axis directions.

4. MODEL CORRELATIONS

In addition to the individual model results discussed in the preceding section, Table 2 contains the same key results characterizing the boundary locations and neutral H content for all 27 models. The model numbers refer to the corresponding boundary parameters listed in Table 1. Model 1 stands out from the rest in that neutrals are absent. For the subsonic models 1 and 2 the LISM pressure is dominated by the thermal pressure. All other models are ram pressure dominated. This is among the reasons why the results discussed below cover only a subset of the vast parameter space.

4.1. *Plasma Structure*

When comparing the 27 models, an obvious result is the variation in the size of the heliosphere, as expressed in the location of upwind TS, HP, and BS in Table 2, as well as the distance of the downwind termination shock (TS_d). These distances are set by balancing the solar wind pressure and interstellar pressure (e.g., Holzer 1989). A small heliosphere is caused by a large LISM pressure. Models 2, 3, 11, and 12 are especially large due to a lower LISM plasma ram pressure, namely, a low LISM velocity in the case of models 2, 3, and 11, and a low density for models 11 and 12. Overall, the upstream distances from the Sun to the TS range from 8 to 260 AU, and those to the HP range from 12 to 400 AU (see Table 2). The bow shock of a cool, slow, tenuous LISM (model 11) is as far as 810 AU away from the Sun.

Because the overall system is pressure balanced, the locations (heliocentric distances) of TS, HP, and BS are correlated with one another. Taking all models except model 1 and adding the results of another systematic (as yet incomplete) parameter study with $v = 26.24$ km s^{-1}, the correlation between r_{TS}, the distance of the upwind TS, with the distance of the upwind heliopause r_{HP}, is

$$r_{HP} = (1.39 \pm 0.01)r_{TS}, \qquad (1)$$

obtained with a linear regression analysis after ascribing uncertainties to r_{TS} and r_{HP} due to grid resolution and HP stability. The intercept value of the analysis is consistent with zero. The omitted model 1 ratio $r_{HP}/r_{TS} = 3.3$; the other subsonic case, model 2, is an outlier with a ratio of 1.55. The filled circles in Figure 6 represent each model as a (TS, HP) pair, and the corresponding straight line is the linear fit of equation (1). Model 1 is additionally marked with a cross.

For models with a supersonic LISM, the upwind bow shock r_{BS} is located about twice as far as the heliopause,

$$r_{BS} = (1.95 \pm 0.05)r_{HP}. \qquad (2)$$

A direct correlation between TS and BS yields $r_{BS} = (2.70 \pm 0.09)r_{TS}$. In deriving the BS correlations, models 3 and 11 were excluded as the largest models; the above relation underpredicts the BS distance of models 3 and 11 by 81 and 114 AU, respectively. Figure 6 shows the model (TS, BS) pairs as triangles. In contrast to the excellent HP data fit, the BS locations are more scattered around their straight line fit. For the smaller heliospheres, the BS lies systematically more inward than predicted from the TS location via the proportionality fit (eq. [2]) and apparently obeys a different linear relation.

For the interstellar ram-pressure-dominated models considered here, the upwind-downwind asymmetry of the TS is essentially constant. Excluding the rocket-shaped models that have a triple point in their TS, the relation for the downwind distance $r_{TS,d}$ of the TS is
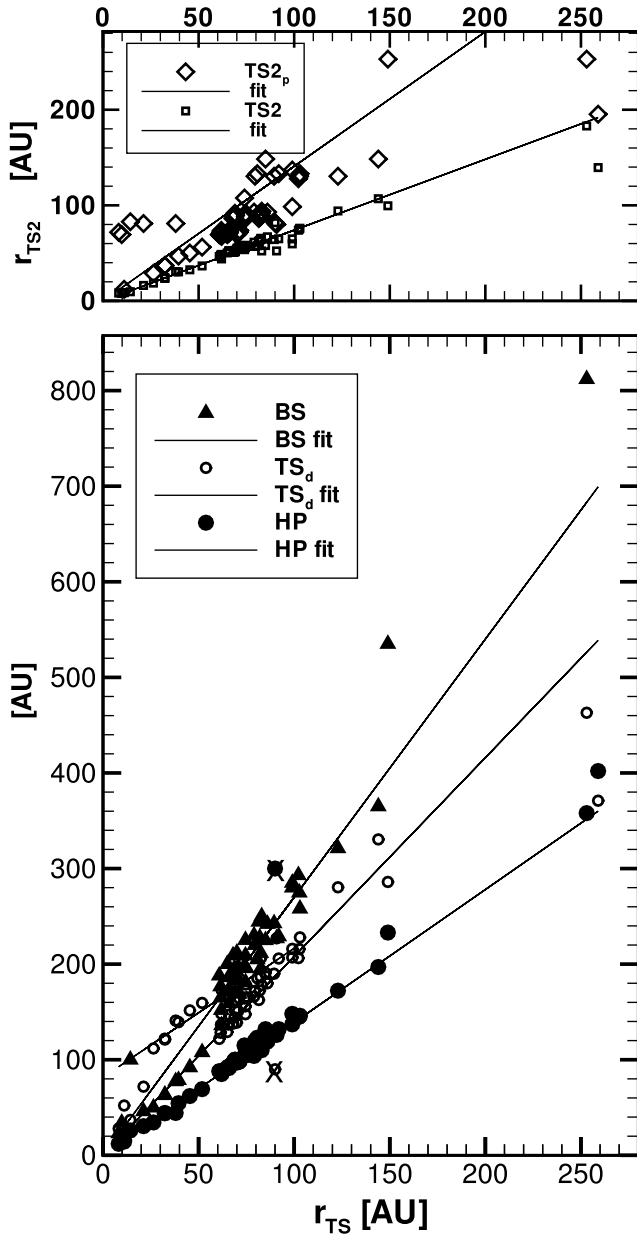
$$r_{TS,d} = (2.08 \pm 0.04)r_{TS}. \qquad (3)$$

FIG. 6.—Correlation between the upwind termination shock location r_{TS} and other distances, including, in the bottom panel, the upwind heliopause HP (*circles*), the upwind bow shock (*triangles*), and the tailward TS distance (*open circles*), which are all model results. Model 1 results are marked with a cross. The top panel shows the TS correlations with the distance r_{TS2} theoretically derived from plasma pressure balance (*diamonds*) and from total pressure balance (*squares*), together with empirical linear fits. Note the aspect ratio of 2 : 1 in both panels. [See the electronic edition of the Journal for a color version of this figure.]

The appearance of a triple point in the remaining models clearly yields a different dependence, namely,

$$r_{TS,d} = (1.35 \pm 0.12)r_{TS} + (82 \pm 7) \text{ AU}. \qquad (4)$$

Again, these fits are shown in Figure 6, with open circles representing their corresponding model data. Both subsonic models 1 and 2 are outliers and were omitted. They obey a different asymmetry law than the rest of the models, stemming from the qualitatively different pressure distribution along the HP in the absence of a bow shock. Model 11 is an outlier with an $r_{TS,d}$

smaller by 63 AU than predicted by the above relation. For small heliospheres, relation (3) fits the high-density cases 15–17 well, but underpredicts the asymmetry of models 14 and 27, which, due to their high velocity, might be on their way to the rocket-shaped cases. The mentioned outliers are not included in the factors of equations (3) and (4). The pressure distribution in the rocket-shaped cases goes hand in hand with a more inward location of the bow shock; the models for which the BS location is inconsistent with equation (2) are the ones for which the heliosphere is of that shape.

In the supersonic solar wind, the total pressure is dominated by the plasma ram pressure. Since most of the kinetic energy of the solar wind is converted into heat at the termination shock, it is effectively the upstream solar wind ram pressure that balances the total interstellar pressure $P_{tot} = P_{pl} + \rho_p v^2 + P_H + \rho_H v^2$, the sum of plasma thermal and ram pressure and neutral H thermal and ram pressure. Hence, a simple one-dimensional pressure balance would be achieved, assuming constant solar wind velocity v_{SW} and an r^{-2} dependence of the density for the supersonic solar wind region, at a radial distance of

$$\frac{r_{pb}}{r_1} = \sqrt{\frac{P_1}{P_{tot}}}, \qquad (5)$$

where $P_1 = \rho_1 v_{SW}^2$ is the solar wind ram pressure, and ρ_1 the solar wind density, both taken at $r_1 = 1$ AU. This basic pressure balance distance assumes that all kinetic energy is converted into heat at the TS. Improving on this by using the Rankine-Hugoniot relations together with treating the heliosheath and interstellar flows as incompressible, and assuming the ISM to be at rest in the heliocentric frame, the TS is calculated to be at (Zank 1999)

$$r_{TS1} = \sqrt{\frac{\gamma + 3}{2(\gamma + 1)}} r_{pb} = \sqrt{\frac{7}{8}} r_{pb}, \qquad (6)$$

where γ is the ratio of specific heats and is set to 5/3 in the second equality, as well as for all the models in this paper.

Suess & Nerney (1990) have calculated the case of an ISM that is moving with respect to the Sun, in which the nose TS position calculated from equation (6) is corrected by a weak dependence on the ratio of interstellar (v) and solar wind velocities,

$$r_{TS2} = \sqrt{\frac{2}{\gamma + 1}} r_{pb} \left[\frac{(\gamma + 1)^2}{4\gamma} \left(1 - \frac{v^2}{v_{SW}^2} \right) \right]^{(\gamma/2)/\gamma - 1}$$
$$= \frac{16}{5} \frac{1}{\sqrt{3\sqrt{15}}} r_{pb} \left(1 - \frac{v^2}{v_{SW}^2} \right)^{5/4}. \qquad (7)$$

For $\gamma = 5/3$, the numerical factors of equations (6) and (7) agree with each other to within 0.4%, and the extra velocity-related factor of equation (7) represents a non-negligible reduction in r_{TS2} compared to r_{TS1} only for high-velocity ISM cases, such as model 14 of this paper (an 8% reduction in this case).

A number of assumptions enter into the derivation of equations (6) and (7). Among them is that these formulas are only valid for a subsonic ISM, with neutral H absent, and P_{tot} should be dominated by the ISM thermal plasma pressure. However, the validity of equations (6) and (7) can be extended to the supersonic LISM case, because an interstellar bow shock will convert the flow to subsonic speeds. It is therefore possible to admit the sum of all plasma pressure contributions into P_{tot} of equation (5).

If neutral H were tightly coupled to the plasma (i.e., if the mean free paths were very short compared to typical heliospheric length scales), then the neutral H pressure contributions can justifiably be included in P_{tot} as well. However, the neutral-plasma coupling is neither zero nor very strong, so the solar wind/LISM pressure balance for the heliospheres modeled in this paper is more complicated.

The 27 models show a correlation between r_{TS2} and the up-wind TS location (and consequently, the upwind HP and BS; eqs. [1] and [2]). We present here two of the r_{TS2} distance estimates. One (r_{pl}) is obtained by using solely the LISM plasma pressure in equations (5) and (7) ($P_{tot,pl} = P_{pl} + \rho_p v^2$), effectively neglecting neutral H altogether. The alternative distance prediction r_{min} uses $P_{tot} = P_{tot,pl} + P_H + \rho_H v^2$, taking the entire pressure contribution of neutral H into account as well. The correlations are

$$r_{TS} = (0.71 \pm 0.08)r_{pl}; \; r_{pl} = r_{TS2}\left(P_{tot,pl}\right) \quad (8)$$

$$r_{TS} = (1.35 \pm 0.02)r_{min}; \; r_{min} = r_{TS2}\left(P_{tot}\right). \quad (9)$$

The data and the regression fits are shown in Figure 6 (top) with diamonds and squares, respectively. The plasma-only correlation (diamonds; eq. [8]) is poor and, especially, pairing models 3 with 11, and 26 with 27, shows that the same plasma total pressure does lead to different heliospheres, depending on the neutral contribution. In addition, the high-density cases 15–17 are complete outliers (as are 26 and 27) for which the plasma pressure alone overpredicts the heliospheric size. For the inclusive correlation (squares; eq. [9]), it is not necessary to exclude any of the supersonic heliospheres, in particular, not models 15–17. Only model 2 is an outlier, but not model 1.

The predicted and modeled TS distances in the plasma-only relation (8) scatter around the fit too much, and neutral-dominated models are excluded outright. The deviations from the predicted locations indicate changes to the pressure balance due to charge exchange with neutral H. The pressure balance gets shifted inward by pickup ion production in the supersonic solar wind that reduces the supersonic wind speed and hence its ram pressure. On the other hand, the TS pressure balance can get shifted outward by other effects, among them the deceleration of the outer heliosheath plasma by charge exchange with secondary neutrals. Relation (9) has a much smaller scatter and therefore is better suited to predict r_{TS}, with the caveat that the neutral-plasma interaction drives the neutrals out of equilibrium, and pressure balance can only be described by an empirical factor of 1.35.

This study is focusing solely on the variation of interstellar boundary parameters and the heliospheric response. While we do not wish to study the question of different solar wind conditions on the heliosphere here, it is interesting to note that all the results so far only depend on P_1, the solar wind ram pressure at 1 AU, and that the locations of TS, HP, and BS are dictated by a pressure balance between solar wind and LISM, with empirical correction factors. In reality, the solar wind is time dependent on an 11 yr cycle and on smaller, episodic timescales. The variation in solar wind ram pressure leads to small variations in the heliospheric boundary locations (e.g., Zank & Müller 2003; Izmodenov et al. 2005) that are qualitatively consistent with equation (9). Similarly, the increased ram pressure in polar directions from the fast polar wind during solar minimum results in larger heliospheric distances in these directions as compared to isotropic slow solar wind (Pauls & Zank 1997; Tanaka & Washimi 1999). An example of the reaction of the heliosphere to different solar wind ram pres-
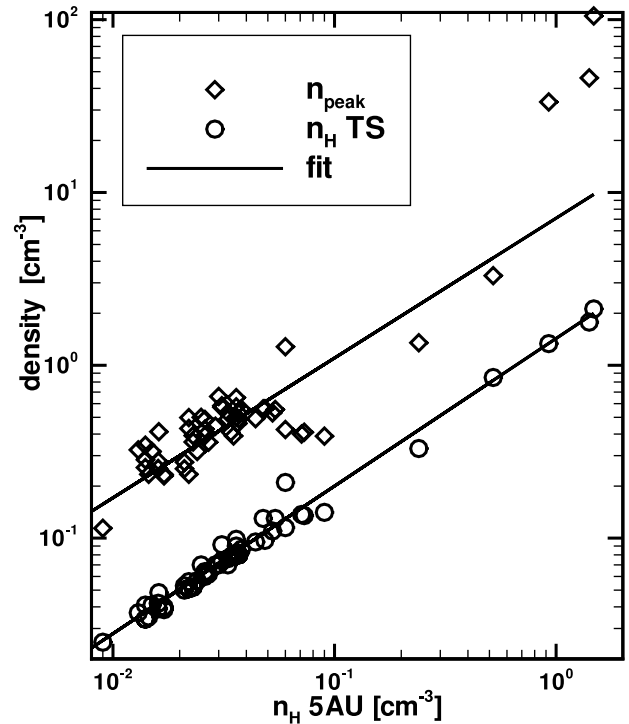

Fig. 7.—Correlations between the neutral H density at 5 AU upwind, and at the TS (circles) and the peak density inside the hydrogen wall, max [n_H(wall)] (diamonds). [See the electronic edition of the Journal for a color version of this figure.]

sures while holding the ISM environment constant is the comparison of models 22–24 in Table 2, where the boundaries move outward for a ram pressure increase (model 24), but do not change for a doubling of the solar wind thermal pressure (model 23).

Recent investigations of astrospheres around other cool main-sequence stars (Müller et al. 2001; Wood et al. 2002, 2005a) use a range of stellar wind ram pressures P_1 that are different from the solar wind, but a modeling strategy identical to the one for the heliosphere. A cursory analysis of these models (plots not shown here) shows that equations (1)–(9) hold also for all these cases within the stated accuracy. This result underscores the argument of pressure balance and extends the results of this section to other ram pressure regimes such as for astrospheres carved out of the ISM by coronal stellar winds.

4.2. Heliospheric Neutral Hydrogen

The density $n_{TS}(H)$ of neutral hydrogen that crosses the termination shock at the upwind stagnation axis varies over a considerable range in the 27 models, from 0.01 to 0.33 cm^{-3}, with four larger values between 0.9 and 2 cm^{-3} for the high-density models 15–17 and 27. The filtration ratio f is the neutral density at the TS divided by the interstellar neutral density $n(H^0)$, well upstream of the BS (to avoid contamination by component 2 and 3 neutrals), and these relative values vary from 0.1 to 0.6, with a few higher values, 0.7–1.0, for higher velocities. The filtration is listed as f_{TS} in Table 2 for all 27 models, as are similar ratios for the peak hydrogen wall density (f_{peak}) and for the density at 5 AU on the upwind stagnation axis ($f_{5\,AU}$). We choose 5 AU as a fixed reference distance, with the expectation that photoionization is not yet important at this distance.

The neutral hydrogen at the TS comprises original interstellar material and slower secondary neutrals created upwind of the
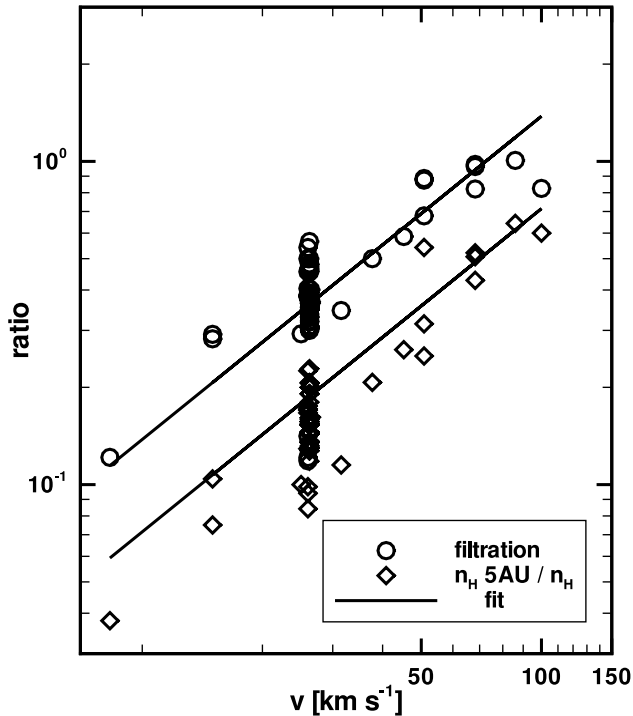
Fig. 8.—Correlation between the filtration ratio $f = n_{TS}(H)/n(H^0)$ and the interstellar velocity v (*circles*), and correlation of the 5 AU density ratio $n_{5\,AU}(H)/n(H^0)$, with v (*diamonds*). The solid lines are linear fits, while the plot itself is double-logarithmic. [*See the electronic edition of the Journal for a color version of this figure.*]

HP, which form the hydrogen wall. After crossing the HP, these neutrals get depleted in the heliosheath by charge exchange, which replaces them with neutrals mostly in outward directions. For high-velocity models, this loss process starts from a higher HP density so that higher filtration ratios occur (§ 3.4). Both the filtration ratios and the absolute TS neutral densities correlate well with the neutral density $n_{5\,AU}(H)$ at 5 AU. The correlations are

$$n_{TS}(H) = (1.43 \pm 0.02)n_{5\,AU}(H)^{0.85 \pm 0.01} \qquad (10)$$

$$f = (1.55 \pm 0.13)\left[\frac{n_{5\,AU}(H)}{n(H^0)}\right]^{0.72 \pm 0.04}, \qquad (11)$$

where all models have been included in equation (10), and the high-density models 15–17 had to be excluded as outliers in equation (11) (plot not shown). The data and the fit (eq. [10]) are displayed in Figure 7 by circles. This correlation is interesting in that it relates a density at a fixed distance to a density at the TS regardless of the actual distance of the TS. The net loss in the region of the supersonic solar wind is not sensitive to the length of the neutral particle trajectories between the TS and 5 AU because most of the charge exchange relevant to the 5 AU density takes place immediately upwind of that distance, given that the local plasma density is larger with smaller distance, resulting in smaller charge-exchange mean free path lengths.

The peak densities in the hydrogen wall range from $1.1n(H^0)$ to massive hydrogen walls of $7n(H^0)$, corresponding to 0.09–105 cm^{-3} in absolute units. The absolute peak density is weakly correlated to the 5 AU value, as demonstrated by the diamonds in Figure 7. Even on a log-log plot, however, a large scatter of

the results around possible power laws is evident. According to a regression analysis that omits the high-density models 15–17,

$$n_{peak}(H) = (7.1 \pm 1.5)n_{5\,AU}(H)^{0.81 \pm 0.06}. \qquad (12)$$

Nonetheless, the fit is poor. The same problem is encountered when relating the neutral results to the interstellar velocity. There is a general trend of higher neutral densities with higher velocity. Figure 8 shows the filtration results (*circles*) and the relative densities at 5 AU (*diamonds*) plotted against the interstellar velocity. It is evident that any correlation derived from these model results is not unique, as there are many data points around $v \approx 26$ km s^{-1} whose normalized neutral results vary by a factor of 2.7. The fit lines shown in Figure 8 are $f = v/(73 \pm 7$ km s$^{-1})$ and $n_{5\,AU}(H)/n(H^0) = v/(140 \pm 8$ km s$^{-1})$.

We caution that the above relations are likely model dependent, in that using another self-consistent modeling strategy for the heliosphere, such as a particle kinetic model for the neutral H (Baranov & Malama 1993; Müller et al. 2000; Heerikhuisen et al. 2006), might result in different coefficients for relations (1)–(4) and (8)–(12). Short of carrying out a parameter study with these alternate models and comparing the results, it is impossible to incorporate this systematic error into the error estimates of the coefficients given in the above relations.

5. DISCUSSION

5.1. Heliospheric Morphology and Neutrals

We are now in a position to discuss some of the consequences that different interstellar environments have for the solar system and for Earth. There are several models listed in Table 2 representing heliospheres that are so small that the outer planets find themselves beyond the supersonic region of the solar wind, at least for parts of their orbits. As examples, Figures 3 and 5 have the orbits for the gas giants Saturn, Uranus, and Neptune marked in them. An assumption in these plots is that the ISM flow vector is close to the plane of the ecliptic, as is the case in the current environment. For larger angles, the ecliptic TS distances are farther due to the upwind/downwind asymmetry of the heliosphere.

In the high-density case 17 (Fig. 3), Uranus periodically crosses the TS, traverses the hot inner heliosheath, crosses the HP, and spends part of its orbit in the shocked LISM (the outer heliosheath), before crossing the HP again in a reverse course of events. Neptune is always surrounded by hot, shocked plasma (either the solar wind heliosheath and heliotail or the interstellar plasma of the outer heliosheath) and is never upstream of the TS. Similarly, in the high-velocity case of model 25 (Fig. 5), part of Neptune's orbit is in the subsonic solar wind of the heliosheath, and Uranus periodically comes close to the TS.

For planets in the hot inner heliosheath it can be expected that solar wind injection into planetary magnetospheres is more efficient due to increased thermal plasma velocity and solar wind turbulence. Also, the solar wind magnetic field strength is enhanced, and an increased flux in both Galactic cosmic rays and heliospheric energetic particles is to be expected. Planets that cross into the outer heliosheath will be exposed to not quite as hot a plasma, carrying a basically undetermined magnetic field. However, the planet will then be exposed to the increased neutral density of the hydrogen wall. This neutral flow will strike the planetary atmosphere unimpeded and lead to atmospheric drag and other effects (Yeghikyan & Fahr 2004b).

None of the 27 models considered here leads to such dire predictions for Earth's orbit, and extrapolating from equations (7)

and (9) beyond their validity, interstellar densities of 1500 cm^{-3} with moderate interstellar velocities—or a velocity of 345 km s^{-1} with moderate interstellar densities—would be needed to place the TS at 1 AU. It should be expected that both of these numbers are only a qualitative estimate, and that detailed modeling of such heliospheres would have to take into account additional physical processes (Yeghikyan & Fahr 2003, 2004a).

As many models in this paper have an inner boundary at or beyond 1 AU, we want to focus on the reference distance of 5 AU instead, to assess the change in particle environment that occurs with different Galactic environments under the assumption of an unchanging solar wind. At this distance, the solar wind is supersonic for all 27 models. The ratio of interstellar (slow) neutral hydrogen to solar wind protons at 5 AU upwind is between 7% and 25% for the contemporary heliosphere (models 4–10). As already mentioned in § 4.2, this density ratio scales with interstellar velocity, ranging from 2% to 37% (models 2 and 18–24, respectively; model 14: 120%; model 25: 45%), and is highest for the high-density models 14–17 and 27. In particular, there is more than 7 times more neutral H than solar wind protons at 5 AU in models 16 and 17.

Naturally, the increased presence of interstellar H^0 increases the rate of charge exchange and hence the production rate of fast component 3 neutrals, the so-called neutral solar wind (NSW). The NSW density at 5 AU for the contemporary heliospheres is $\approx 4 \times 10^{-4}$ cm^{-3}, but increases to 0.014, 0.018, and 0.023 cm^{-3} for models 15, 16, and 17, respectively. A similar drastic relative NSW increase should occur at Earth orbit for these high-density cases. In contrast, the high-velocity case 25 only yields a five-fold increase of NSW to 0.002 cm^{-3} at 5 AU.

5.2. Cosmic-ray Transport Model

As an application of the results discussed above, we make use of a cosmic-ray transport model for three demonstrative solutions of GCR phase-space density. They are calculated for the interstellar environments corresponding to the Local Bubble, the LIC, and a dense cloud of mostly neutral hydrogen, based approximately on models 1, 9, and 15, respectively. The cosmic-ray transport model we use is discussed in detail in Florinski & Zank (2006), and the reader is referred to that paper for a complete description. Briefly, the plasma flow background obtained from the multifluid code is used to calculate all three components of the heliospheric magnetic field in the azimuthal plane from Faraday's law combined with the zero-divergence condition with a Parker spiral field specified at the inner boundary (Florinski et al. 2003b). The modified field component of Jokipii & Kota (1989) that alters the transport parameters at high heliographic latitude is also included in the model. The interstellar magnetic field plays no role in this model because it fluctuates on scales that are typically much larger than the diameter of the cosmic-ray gyro-orbit and hence has little effect on the particle's trajectories. Next, magnetic turbulent energy $\langle \delta B^2 \rangle$ and the associated turbulence correlation length in the solar wind region are computed from the hydrodynamic model of incompressible turbulence transport (Zank et al. 1996a; Matthaeus et al. 1999). The model assumes that the number of waves propagating parallel and antiparallel to the mean magnetic field are equal and ignores certain wave propagation effects by neglecting the Alfvén speed compared with the mean plasma velocity in the solar wind.

Little is known observationally about the turbulent content of the inner heliosheath, and turbulence transport in that region is poorly understood at present. Here we use a simple assumption that the turbulent ratio $\langle \delta B^2 \rangle / B^2$ and the correlation length are both constant across the termination shock and in the helio-

sheath. This assumption is based on the physics of Alfvén wave transmission through a quasi-perpendicular shock that yields the expression relating the turbulent ratio on the two sides of the shock as (McKenzie & Westphal 1969)

$$\frac{\langle \delta B_2^2 \rangle}{B_2^2} = \frac{(s+1)}{2s} \frac{\langle \delta B_1^2 \rangle}{B_1^2}, \qquad (13)$$

which is not too different from 1 for shocks of moderate strength (compression ratios $s = 2.5$–3.0).

The turbulent content of the solar wind is strongly influenced by the process of Alfvén wave generation by pickup ions as they scatter from the initial ring-beam distribution onto a bisphere in velocity space (Williams & Zank 1994; Isenberg et al. 2003). Because pickup ions are produced in charge transfer collisions between solar wind protons and interstellar hydrogen atoms, changes in neutral density are the principal source of turbulence variability. The latter translates into variations in the amount of GCR modulation through an appropriate diffusion model. We use the quasi-linear theory (QLT; e.g., Jokipii 1966) for the parallel component of the diffusion tensor and the nonlinear guiding center (NLGC) theory (Matthaeus et al. 2003) for the perpendicular component. The former is governed by the fluctuations with wavevectors oriented parallel to the mean magnetic field (the slab component), while the latter is determined by the fluctuations orthogonal to the field (the two-dimensional component). We assume that slab fluctuations contribute 10% of the total energy, with the two-dimensional component making up the rest, which is in agreement with the observed ratio (Bieber et al. 1996).

Both QLT and NLGC require a specification of the reduced (one-dimensional) turbulent spectrum. The power spectrum measured in the solar wind at low latitudes consists of a flat energy range followed by a Kolmogorov inertial range with $k^{-5/3}$ (e.g., Bieber et al. 1994), while some observational evidence points to a k^{-1} dependence at high latitudes (Horbury & Balogh 2001). The low end of the turbulence spectrum is likely to be populated by structures (shocks and discontinuities) that may be responsible for the modulation of very high energy (above 1 GeV) particles. Accordingly, we use two forms of the power spectrum, identical in the inertial range, but having a different spectral index in the energy range: 0 (diffusion model I) and -1 (diffusion model II). As discussed in Florinski & Zank (2006), the first model emphasizes modulation in the heliosheath region, while model II is dominated by solar wind modulation. Because the amount of modulation in the heliosheath is not known at present, we use two plausible models to cover the full range of possibilities.

5.3. Cosmic-ray Modulation Results

The different sizes of the heliosphere, as well as the different particle distributions, will affect the modulation of GCRs as they pass from the ISM through the heliosphere into interplanetary space and to Earth. The GCR transport coefficients depend on the heliospheric magnetic field, as well as on the level of plasma turbulence. While the magnetic field geometry, its strength, and the properties of solar wind turbulence (especially in the heliosheath) are far from having been studied conclusively, theoretical models of cosmic-ray transport can be constructed on the basis of known physics (Florinski et al. 2003b; Florinski & Zank 2006). Here we perform a series of computer simulations of GCR modulation in the global heliosphere for models 1 (heliosphere in the Local Bubble), 9 (contemporary heliosphere), and 15 (a high-density cloud encounter).
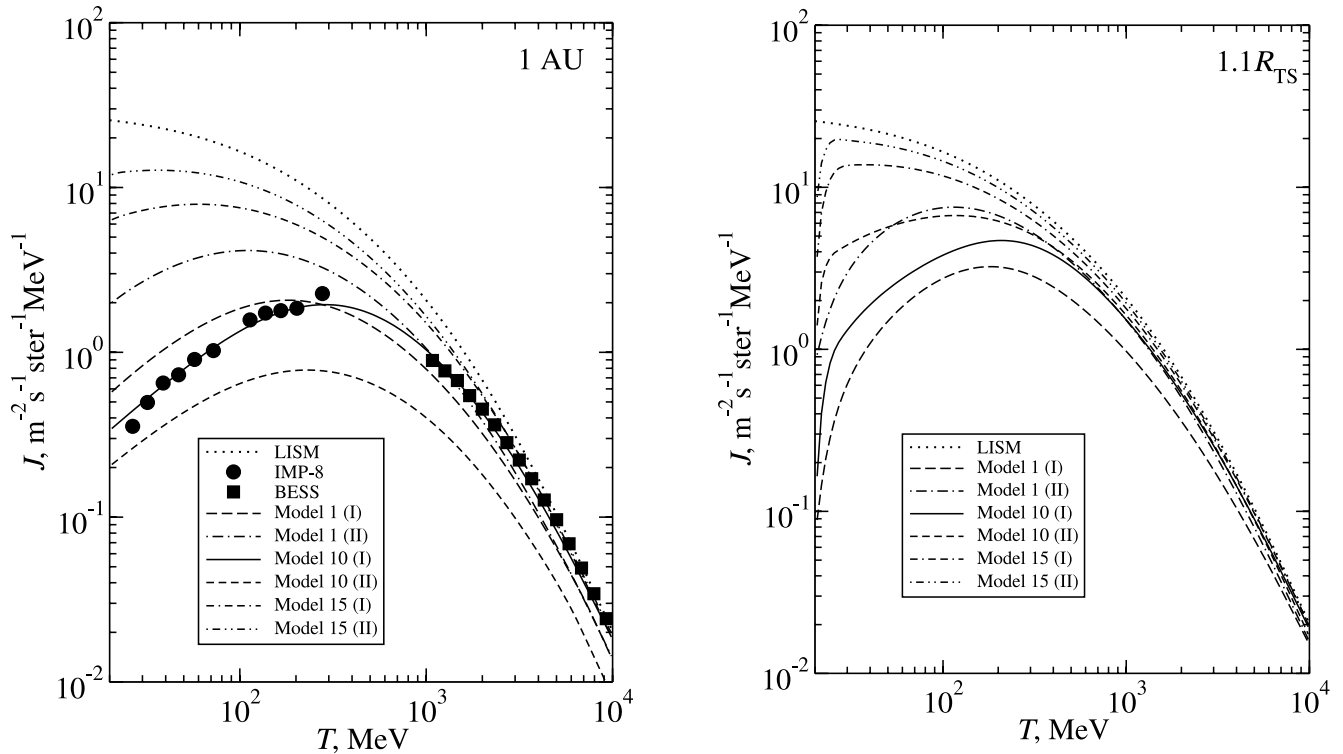
Fig. 9.—GCR proton differential spectra at 1 AU (*left*) and just beyond the termination shock (*right*) in the apex direction for the three interstellar environments represented by models 1, 9, and 15. The ISM GCR spectrum assumed at the external boundary (Ip & Axford 1985) is shown with a solid black line. The roman numerals following the model number refer to turbulence evolution models I and II. 1 AU spectra observed during the time around the 1995 solar minimum are shown for comparison. The low-energy data are from *IMP 8* satellite observations (McDonald 1998), while high-energy data are from BESS balloon measurements (Sanuki et al. 2000). [*See the electronic edition of the Journal for a color version of this figure.*]

A thicker heliosheath such as in model 1 could in principle be expected to yield stronger modulation of GCRs (i.e., a lower particle flux arriving at Earth). However, the level of magnetic field turbulence production, which in turn depends partly on PUI production, can be less efficient in low-density environments. Figure 9 shows the high-energy proton GCR spectra for the three cases (models 1, 9, and 15) calculated with diffusion models I and II. The right panel of this figure shows particle intensity at the termination shock, thus demonstrating the effect of heliosheath modulation. Because low-energy GCR protons typically do not reach 1 AU, we focus on the high-energy end of the spectra.

It follows from our model calculations that the GCR environment at Earth for the Local Bubble scenario (model 1) would have been less intense than at present if diffusion model I was correct, or, surprisingly, more intense with model II diffusion coefficients. The latter is a consequence of the large GCR mean free path predicted by the second diffusion model for the solar wind region in model 1 in the absence of PUI turbulence driving. In both cases, the cumulative heliosheath GCR modulation is more important for the Local Bubble environment than for the contemporary heliosphere. This is a combined effect of a stronger TS, a larger decrease in the radial mean free path across the shock, and a thicker heliosheath.

For an encounter with a high-density cloud (model 15), the heliospheric GCR shielding is much less effective than in the contemporary heliosphere, such that the high-energy part of the GCR spectrum approaches the one assumed for the pristine LISM. Here the opposing effects of a relatively large heliosheath diffusion coefficient combined with a much smaller extent of the modula-

tion cavity, and enhanced PUI turbulence driving in the solar wind, result in a significant reduction in the heliospheric shielding of GCRs. The predicted cosmic-ray intensity increase at Earth is between 1.4–2.4 (model I) and 4.1–7.6 (model II) in the energy interval between 300 MeV and 1 GeV.

In addition to GCRs, the distribution of anomalous cosmic rays that are accelerated at the TS will depend on the background neutral density and the strength and distance of the TS (Florinski et al. 2003a). Together, the cosmic-ray environment at Earth influences the terrestrial magnetosphere, as well as climate, atmosphere, and biology (e.g., Scherer 2000; Yeghikyan & Fahr 2004b; Frisch et al. 2005).

6. CONCLUSIONS

On its path through the galaxy, the Sun has encountered (and will encounter) different interstellar environments. This motivates a parameter study to investigate the response of the heliosphere to these changing conditions under the assumption of a constant solar wind. For conditions that are not too far from the contemporary LISM environment, the following findings emerge from analyzing 27 self-consistent multifluid models.

1. Allowing generous assumptions about the LIC morphology, the LIC column density toward nearby stars indicates that the Sun first encountered the LIC gas within the past 40,000 yr, and the CLIC within the past $\sim$60,000/$\tilde{f}$ years (where $\tilde{f}$ represents the fraction of space filled by the CLIC). The Sun is expected to exit the LISM gas cloudlet, which is characterized by the common LIC velocity, sometime within the next $\sim$0–4000 yr. In general, passage through interstellar clouds will lead to variations

in the heliosphere boundary conditions over timescales possibly as short as 10^3 yr. Nearby ISM generally resembles low column density ISM observed elsewhere.

2. The size of the heliosphere is determined by the balance of solar wind and interstellar pressure. For the investigated parameter range, in which the LISM is mostly ram pressure dominated, the upwind termination shock distance can be estimated by equation (9), using equations (5) and (7). This relation is derived from a pressure balance argument modified by an empirical factor expressing the efficiency of the neutral pressure contribution to the overall interstellar pressure.

3. Heliocentric distances of interest such as the heliopause, the bow shock, or the upwind and downwind termination shock scale linearly with each other (e.g., $r_{HP} = 1.39 r_{TS}$, $r_{BS} = 1.95 r_{HP}$). Therefore, when the upwind termination shock distance is predicted in an absolute way as above, the other distances can be predicted as well. However, the scalability and predictability of the heliosphere size with these relations are only applicable to parameter sets in which the LISM flow is supersonic. The subsonic cases, when the Sun is surrounded by hot plasma or alternately when the Sun and the surrounding interstellar cloud are comoving in space, obey a different set of correlations and are generally more difficult to model numerically.

4. For low interstellar velocities, the heliosheath and heliotail plasma are subsonic throughout, and the ratio of downwind to upwind termination shock distance (TS asymmetry) is 2.1. For higher velocities, the heliosphere assumes a rocket shape, with a modified pressure balance in the downwind directions.

5. Neutral hydrogen results such as the filtration ratio, the peak hydrogen wall density, or the density at 5 AU upwind of the Sun, correlate with one another. Their absolute value is weakly correlated with the interstellar velocity with which the neutrals arrive at the respective heliosphere, as the charge-exchange mean free path depends on this velocity, and higher velocities shorten the heliocentric distances to the heliospheric boundaries.

6. For encounters with a high-density interstellar cloud (~ 15 cm^{-3}, about 50 times the contemporary value), the particle fluxes arriving at Earth orbit, including interstellar neutrals, neutral solar wind, and cosmic rays, will increase markedly. These changes potentially affect Earth's atmosphere and its climate. The changes in particle fluxes due only to a higher interstellar velocity are less pronounced.

7. For the period when the Sun was embedded in the Local Bubble, particle fluxes were reduced substantially. Secondary particles such as anomalous cosmic rays and neutral solar wind were entirely absent, and the Galactic cosmic-ray flux arriving at Earth was comparable to the contemporary flux, or even reduced, depending on the modulation model.

REFERENCES

Alexashov, D., & Izmodenov, V. V. 2005, A&A, 439, 1171
Baranov, V., & Malama, Y. 1993, J. Geophys. Res., 98, 15157
Bieber, J. W., Matthaeus, W. H., Smith, C. W., Wanner, W., Kallenrode, M.-B., & Wibberenz, G. 1994, ApJ, 420, 294
Bieber, J. W., Wanner, W., & Matthaeus, W. H. 1996, J. Geophys. Res., 101, 2511
Dehnen, W., & Binney, J. J. 1998, MNRAS, 298, 387
Fite, W., Smith, A., & Stebbings, R. 1962, Proc. R. Soc. London A, 268, 527
Florinski, V., & Zank, G. P. 2006, in Solar Journey, ed. P. C. Frisch (New York: Springer), in press
Florinski, V., Zank, G. P., & Axford, W. I. 2003a, Geophys. Res. Lett., 30, SSSC 5-1
Florinski, V., Zank, G. P., & Pogorelov, N. V. 2003b, J. Geophys. Res., 108, SSH 1-1
Frisch, P. C. 1981, Nature, 293, 377
———. 1993, ApJ, 407, 198
———. 1994, Science, 265, 1423
———. 1997, preprint (astro-ph/9705231)
———. 2003, ApJ, 593, 868
———. 2004, in AIP Conf. Proc. 719, Physics of the Outer Heliosphere, ed. V. Florinski, N. V. Pogorelov, & G. P. Zank (Melville: AIP), 404
Frisch, P. C., Grodnicki, L., & Welty, D. E. 2002, ApJ, 574, 834
Frisch, P. C., Müller, H.-R., Zank, G. P., & Lopate, C. 2005, in Astrophysics of Life, ed. M. Livio, N. Reid, & W. Sparks (New York: Cambridge Univ. Press), 21
Frisch, P. C., & Slavin, J. D. 2003, ApJ, 594, 844
———. 2006, in Solar Journey, ed. P. C. Frisch (Berlin: Springer), in press
Frisch, P. C., & York, D. G. 1986, in The Galaxy and the Solar System (Tucson: Univ. Arizona Press), 83
Gry, C., & Jenkins, E. B. 2001, A&A, 367, 617
Hebrard, G., Mallouris, C., Ferlet, R., Koester, D., Lemoine, M., Vidal-Madjar, A., & York, D. 1999, A&A, 350, 643
Heerikhuisen, J., Florinski, V., & Zank, G. P. 2006, J. Geophys. Res., 111, A06108
Heiles, C. 2001, ApJ, 551, L105
Heiles, C., & Troland, T. H. 2003a, ApJS, 145, 329
———. 2003b, ApJ, 586, 1067
Holberg, J., Bruhweiler, F., & Dobie, M. B. P. D. 1999, ApJ, 517, 841

Holzer, T. E. 1989, ARA&A, 27, 199
Horbury, T. S., & Balogh, A. 2001, J. Geophys. Res., 106, 15929
Ip, W.-H., & Axford, W. I. 1985, A&A, 149, 7
Isenberg, P. A., Smith, C. W., & Matthaeus, W. H. 2003, ApJ, 592, 564
Izmodenov, V. V., Malama, Y. G., & Ruderman, M. S. 2005, A&A, 429, 1069
Jokipii, J. R. 1966, ApJ, 146, 480
Jokipii, J. R., & Kota, J. 1989, Geophys. Res. Lett., 16, 1
Linsky, J., & Wood, B. 1996, ApJ, 463, 254
Lockman, F. J., & Gehman, C. S. 1991, ApJ, 382, 182
Matthaeus, W. H., Qin, G., Bieber, J. W., & Zank, G. P. 2003, ApJ, 590, L53
Matthaeus, W. H., Zank, G. P., Smith, C. W., & Oughton, S. 1999, Phys. Rev. Lett., 82, 3444
McDonald, F. B. 1998, Space Sci. Rev., 83, 33
McKenzie, J. F., & Westphal, K. O. 1969, Planet. Space Sci., 17, 1029
Müller, H.-R., & Zank, G. P. 2004, J. Geophys. Res., 109, A07104
Müller, H.-R., Zank, G. P., & Lipatov, A. S. 2000, J. Geophys. Res., 105, 27419
Müller, H.-R., Zank, G. P., & Wood, B. 2001, ApJ, 551, 495
Nerney, S., Suess, S. T., & Schmahl, E. J. 1993, J. Geophys. Res., 98, 15169
Pauls, H., & Zank, G. P. 1997, J. Geophys. Res., 102, 19779
Raisbeck, G., Yiou, F., Bourles, D., Lorius, C., Jouzel, J., & Barkov, N. 1987, Nature, 326, 273
Redfield, S., & Linsky, J. L. 2002, ApJS, 139, 439
———. 2004a, ApJ, 602, 776
———. 2004b, ApJ, 613, 1004
Sanuki, T., et al. 2000, ApJ, 545, 1135
Scherer, K. 2000, in The Outer Heliosphere, ed. K. Scherer, H. Fichtner, & E. Marsch (Katlenburg-Lindau: Copernicus), 327
Slavin, J. D., & Frisch, P. C. 2002, ApJ, 565, 364
Snowden, S. L., et al. 1997, ApJ, 485, 125
Sonett, C. P., Morfill, G. E., & Jokipii, J. R. 1987, Nature, 330, 458
Stanimirović, S., & Heiles, C. 2005, ApJ, 631, 371
Suess, S. T., & Nerney, S. 1990, J. Geophys. Res., 95, 6403
Tanaka, T., & Washimi, H. 1999, J. Geophys. Res., 104, 12605
Vallerga, J. 1998, ApJ, 497, 921
Welty, D. E., Hobbs, L. M., Lauroesch, J. T., Morton, D. C., Spitzer, L., & York, D. G. 1999, ApJS, 124, 465
Welty, D. E., Jenkins, E. B., & Raymond, J. 2002, ApJ, 579, 304
Williams, L. L., & Zank, G. P. 1994, J. Geophys. Res., 99, 19229

Wimmer-Schweingruber, R. F., & Bochsler, P. 2000, in AIP Conf. Proc. 528, Acceleration and Transport of Energetic Particles Observed in the Heliosphere, ed. R. A. Mewaldt et al. (New York: AIP), 270

Witte, M. 2004, A&A, 426, 835

Witte, M., Banaszkiewicz, M., & Rosenbauer, H. 1996, Space Sci. Rev., 78, 289

Wood, B., Linsky, J., Müller, H.-R., & Zank, G. P. 2001, ApJ, 547, L49

Wood, B., Linsky, J., & Zank, G. P. 2000a, ApJ, 537, 304

Wood, B., Müller, H.-R., & Zank, G. P. 2000b, ApJ, 542, 493

Wood, B., Müller, H.-R., Zank, G., & Linsky, J. 2002, ApJ, 574, 412

Wood, B., Müller, H.-R., Zank, G., Linsky, J., & Redfield, S. 2005a, ApJ, 628, L143

Wood, B. E., Redfield, S., Linsky, J. L., Müller, H. R., & Zank, G. P. 2005b, ApJS, 159, 118

Yeghikyan, A., & Fahr, H. 2003, Ann. Geophys., 21, 1263

———. 2004a, A&A, 415, 763

———. 2004b, A&A, 425, 1113

Zank, G. P. 1999, Space Sci. Rev., 89, 413

Zank, G. P., & Frisch, P. C. 1999, ApJ, 518, 965

Zank, G. P., Matthaeus, W. H., & Smith, C. W. 1996a, J. Geophys. Res., 101, 17093

Zank, G. P., & Müller, H.-R. 2003, J. Geophys. Res., 108, SSH 7-1

Zank, G. P., Pauls, H. L., Williams, L. L., & Hall, D. T. 1996b, J. Geophys. Res., 101, 21639